Electronic Supporting Information

---

for

"On demand" triggered crystallization of $CaCO_3$ from solute precursor species stabilized by the water-in-oil microemulsion

Tomasz M. Stawski[ab], Teresa Roncal-Herrero[cd], Alejandro Fernandez-Martinez[e], Adriana Matamoros-Veloza[bf], Roland Kröger[c], Liane G. Benning[abg]

[a]German Research Centre for Geosciences, GFZ, Interface Geochemistry, Potsdam, Germany; [b]School of Earth and Environment, University of Leeds, LS2 9JT, Leeds, UK; [c]Department of Physics, University of York, YO10 5DD, York, UK; [d]current affiliation: School of Chemical and Process Engineering, University of Leeds, LS2 9JT, Leeds, UK; [e]Univ. Grenoble Alpes, Univ. Savoie Mont Blanc, CNRS, IRD, IFSTTAR, ISTerre, 38000 Grenoble, France; [f]current affiliation: School of Mechanical Engineering, University of Leeds, LS2 9JT, Leeds, UK; [g]Department of Earth Sciences, Freie Universität Berlin, Berlin, Germany.

Corresponding authors:

Tomasz M. Stawski; German Research Centre for Geosciences, GFZ, Interface Geochemistry, 14473, Potsdam, Germany; +4933128827511; stawski@gfz-potsdam.de

Roland Kröger; Department of Physics, University of York, YO10 5DD, York, UK; +441904324622; roland.kroger@york.ac.uk

Liane G. Benning; German Research Centre for Geosciences, GFZ, Interface Geochemistry, 14473, Potsdam, Germany; +4933128828970; benning@gfz-potsdam.de

---

Supporting Figures: S1, S2, S3, S4, S5, S6

Supporting Tables: S1, S2

Supporting Experimental Details

Supporting Notes: S1, S2, S3, S4

Supporting References

Supporting Figures

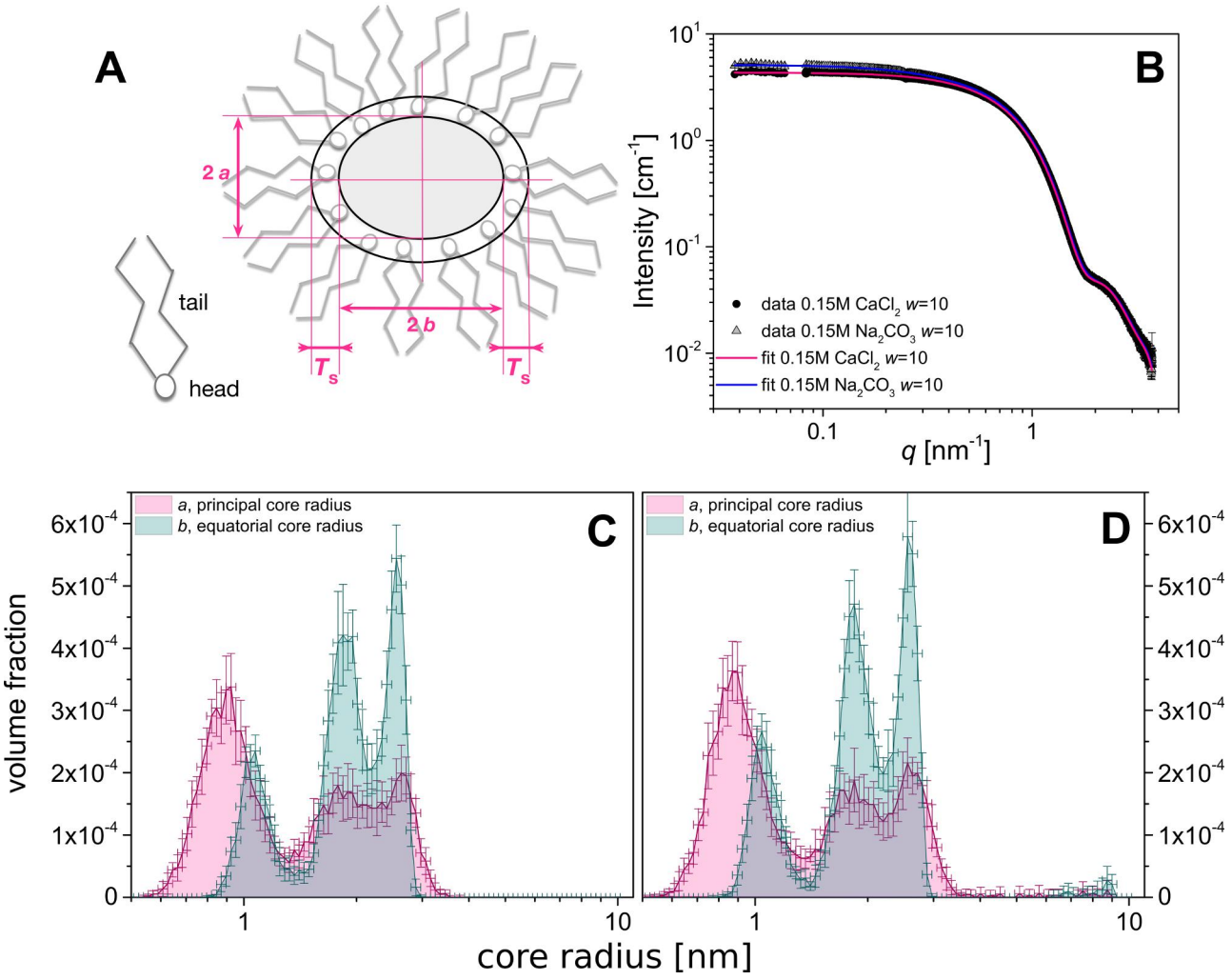

Fig. S1. Structure of the reverse micelles from SAXS. A) Schematic of a reverse micelle as a core-shell aggregate with the surfactant molecules surrounding the water pool. The surfactant's polar heads are located at the interface with the water and they form a shell of a constant thickness T_s. In our convention, the water core has a shape of an ellipsoid of a principal core radius a, and an equatorial core radius b; B) experimental scattering profiles of the $CaCl_2$- and Na_2CO_3 -carrying microemulsions of w=10 and with salt concentrations equalling 0.15 mol/L , together with fitted curves based on the polydisperse core-shell ellipsoid model (see A), in which T_s was constant and given (see Table S1), and a and b were allowed to be affected by the size distribution(s) between 0.5 nm and 100 nm. The resulting form-independent size distributions from the Monte Carlo fitting with MCSAS[1] are shown in: C) for $CaCl_2$-carrying microemulsion and D) for Na_2CO_3-carrying microemulsion. From C and D one can see that both microemulsions had practically the same structure with an average mean radius of the water cores of ~1.7 nm.

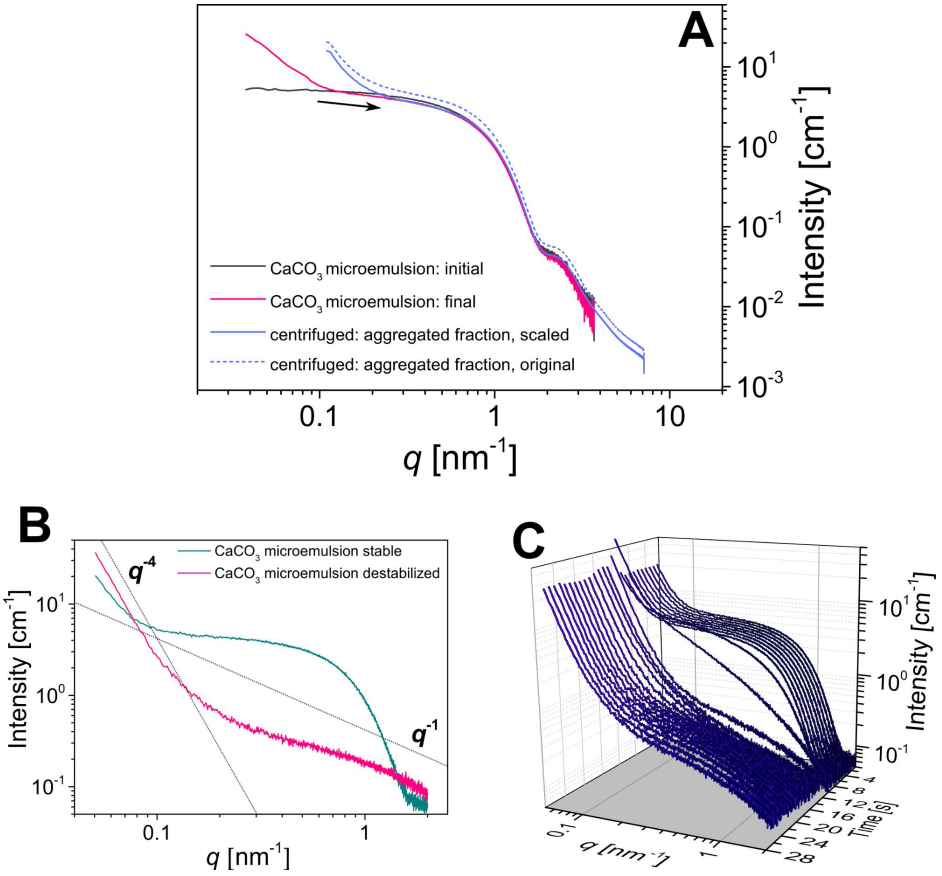

Fig. S2. Scattering profiles of the uncentrifuged, centrifuged, and destabilized $CaCO_3$ microemulsions. A) The centrifugation processes increases the content of aggregated micelles with respect to the non-clustered ones, which is visible by the shift of the low-q intensity increase region towards higher-q (see the arrow). The blue curves were measured at a sample-to-detector distance shorter than the remaining two, hence they cover a slightly different q-range, but the low-q increase region in the blue curves actually extends further to lower scattering vector magnitudes. The intensity in the solid blue curve is scaled with respect to the pink one by a factor of 0.776 times in order to emphasize the fact that the high-q parts of the data overlap perfectly between the pink and blue curves which indicates that internally the aggregates are composed of the same kind of micelles (the original scattering pattern: dashed blue line). The destabilization of the $CaCO_3$ microemulsion occurring upon the ethanol addition; B) comparison of the aged stable and destabilized $CaCO_3$ microemulsion, where the original form factor of the micelle at $q > 0.2$ nm^{-1} (the cyan line) diminishes and completely changes the profile upon the ethanol addition (the pink line) ; the dashed lines indicate characteristic scattering exponents; C) the *in situ* and time-resolved representation of the transition highlighting the changes taking place in the form factor of the micelles; the time axis in reversed.

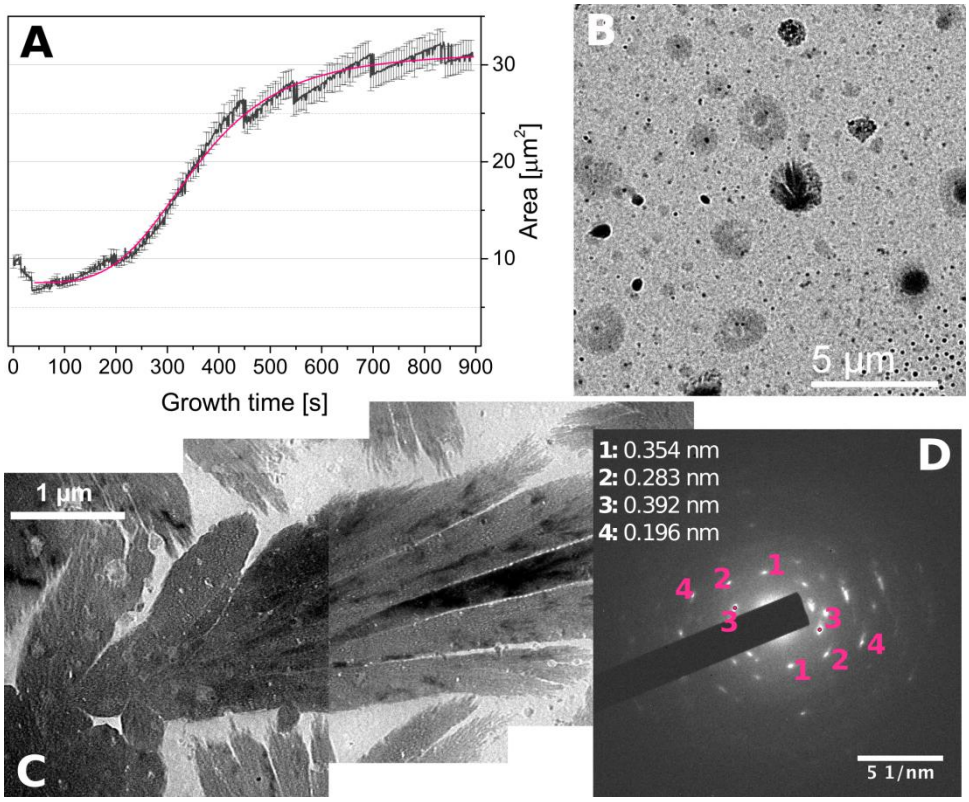

Fig. S3. Destabilization of the $CaCO_3$ microemulsion. A) Time-resolved change in the area of the precipitates in the field of view. B to D: *Ex situ* TEM images and analyses of precipitates formed post ethanol injection on the Si_3N_4 membrane: B) burst globules revealing fan-flower shaped internal contents; C) dendritic fan-shaped morphologies; D) selected area electron diffraction (SAED) from C; Based on the diffraction spots in SAED (pink numbers) and the corresponding *d*-spacing values (white numbers) we identified the precipitated phase as vaterite (Table S2, Fig. S4). Such a diffraction pattern of smeared individual spots (*i.e.,* mosaicity) is best attributed to a structure composed of smaller units, which are preferentially orientated but slightly misaligned with respect to each other. Similar effects can be seen when microemulsion were destabilised *ex situ* during simple drying (see Note S3 and Fig. S5). The time scale in A, correspond to that in the Video S2, where t = 0 s marks the injection of ethanol after the image sequence in Video S1 had been taken.

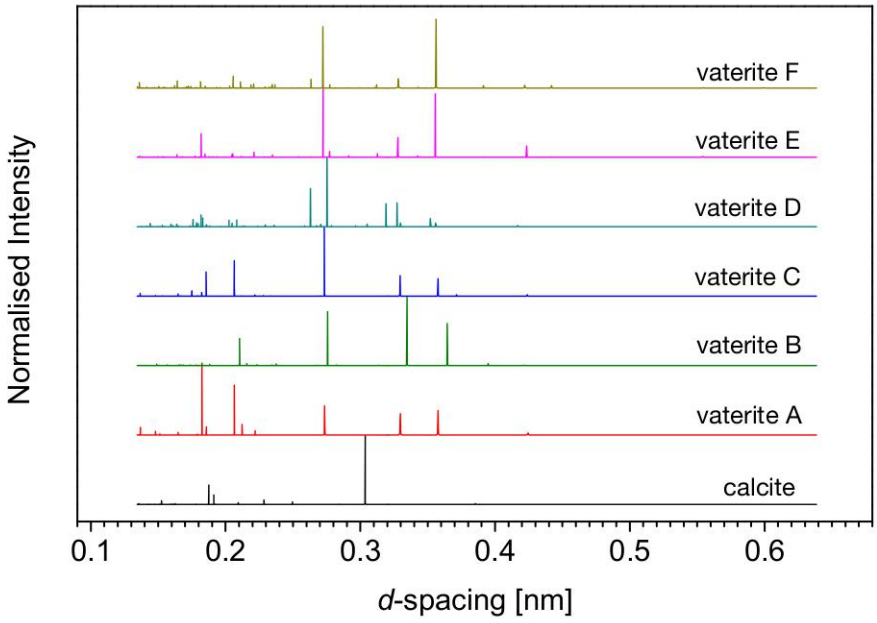

Fig. S4. Simulated[2] diffraction pattern for calcite and vaterite. The patterns were simulated from the structural information summarized in Table S2.

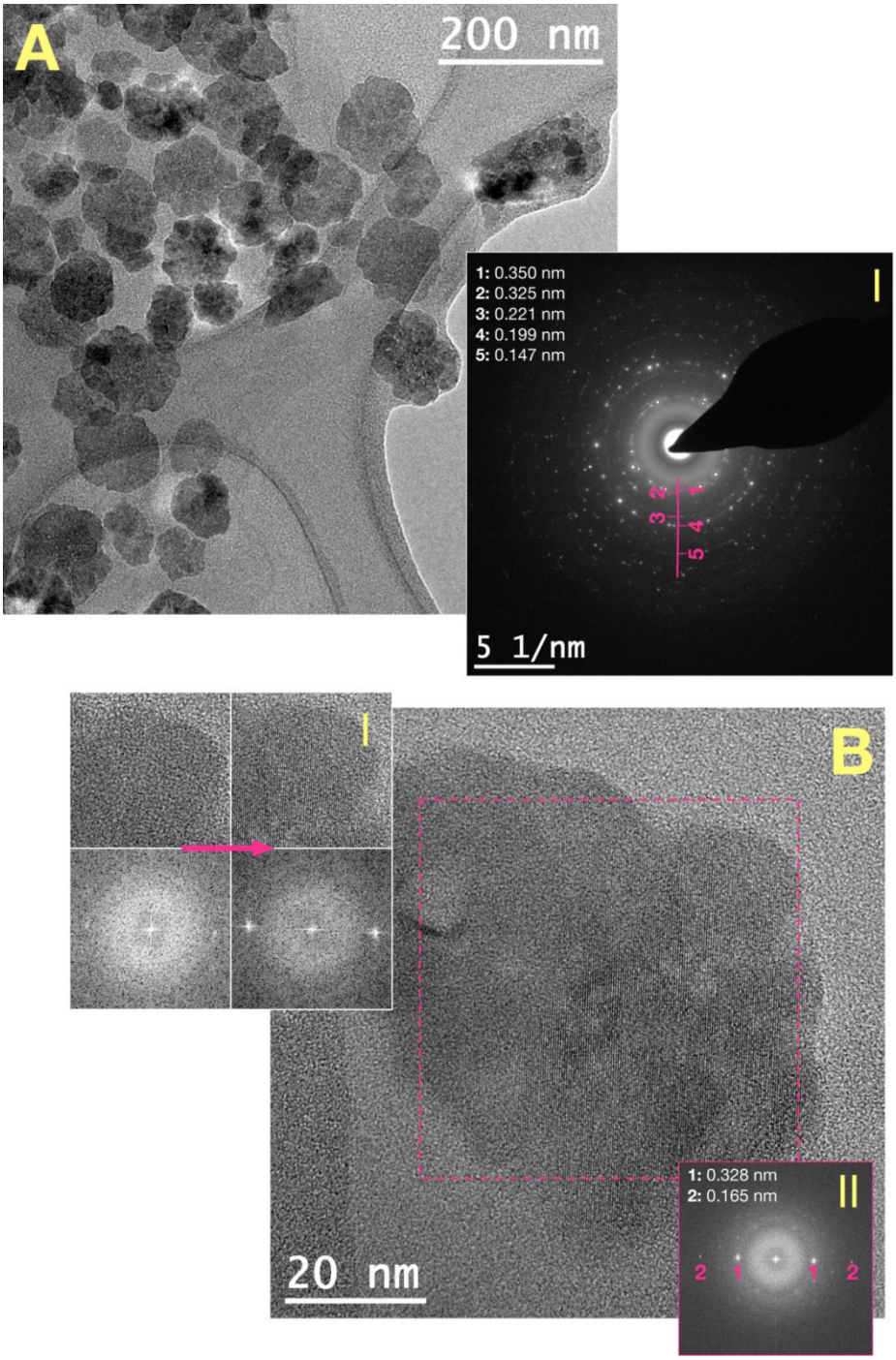

Fig. S5. Solid phases formed post drying (and imaging) of $CaCO_3$ microemulsions. A) TEM micrograph of a dry product obtained from a 0.075 mol/L $CaCO_3$ *w*=10 microemulsion harvested after 3 h after mixing of the individual microemulsions; inset I shows the SAED from the imaged area with a diffraction pattern clearly matching that of vaterite; B) High-resolution micrograph from an aggregate formed under the same conditions as that imaged in A; inset I shows the crystallization induced by the electron beam as illustrated by the sequence of two images from exactly the same area of the aggregate showing more pronounce lattice fringes after longer exposure as documented by the respective fast Fourier transform (FFT) of the two images, with the second image showing higher intensities of the reflections; inset II shows the FFT from the area enclosed by the square (purple dashed line) in B indicating that lattice fringes match those of vaterite.

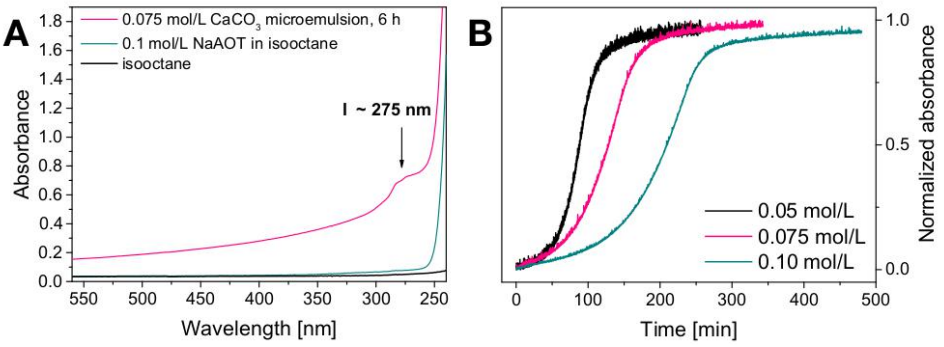

Fig. S6. UV-VIS characterization of the microemulsions. A) The UV-VIS spectrum of a mixed 0.075 mol/L $CaCO_3$ microemulsion of w = 10 reacted for 6 h compared with the selected microemulsions components (as indicated in the legend); these measurements were used to determine the local maximum absorbance at 275 nm. We associated this maximum with the presence of globules (see the main text) and used it as a proxy for the progress of their formation; B) Normalized absorbance as a function of time for three microemulsions of constant w = 10, but with variable [$CaCO_3$] concentration as indicated in the legend.

Supporting Tables

Table S1. Summary of the structural parameters of the reverse micelles.

Polar phase: **reverse micelle's core**	**Ionic surfactant:** **reverse micelle's shell**	**Apolar phase:** **oil medium**
Water ρ_{water} = 334 e^-/nm^3 The presence of dissolved salts at the concentrations used in our experiments increases ρ_{water} by < 2% and is therefore neglected: 0.15 mol/L $CaCl_2$, 1.012 g/cm^3: $\rho_{Ca,aq}$ = 337.4 e^-/nm^3 0.15 mol/L Na_2CO_3, 1.015 g/cm^3: $\rho_{Na,aq}$ = 338.7 e^-/nm^3	NaAOT In SAXS the shell includes only the polar heads. Polar hydrophilic head – essentially sulfonic group and sodium counter ion ρ_{head} = ~850 e^-/nm^3 T_s = ~0.5 nm Apolar hydrophobic tail – essentially succinate group and 2-ethylhexoxy hydrocarbon chains ρ_{tail} = ~250 e^-/nm^3 L = 1.26 nm	Isooctane $\rho_{isooctane}$ = 241 e^-/nm^3

Table S2. Reference crystallographic information for calcite and several vaterite forms.

Phase	**Structure origin**	**Space group**	**Database entry**	**Reference**
calcite	Natural	R -3 c	AMCSD 0000098	[3]
vaterite A	Synthetic	P 63/m m c	AMCSD 0009279	[4]
vaterite B	Theoretical	P 65 2 2	AMCSD 0004854	[5]
vaterite C	Natural	P b n m	AMCSD 0019139	[6]
vaterite D	Synthetic	C 1 2/c 1	AMCSD 0019138	[7]
vaterite E	Theoretical	P 65	AMCSD 0019869	[8]
vaterite F	Theoretical	P 32 2 1	AMCSD 0019870	[8]

Supporting Experimental Details

Microemulsion preparation: expected reaction products and observations

Theoretically, upon inter-micellar ion-exchange, at the local $[Ca^{2+}]$ = 0.075 mol/L and $[CO_3^{2-}]$ = 0.075 mol/L concentrations, the aqueous phase should become supersaturated with respect to calcite (supersaturation index, SI_{Cc} = 4.00), aragonite (SI_{Ar} = 3.85), vaterite (SI_{Vat} = 3.37) and amorphous calcium carbonate, ACC (SI_{ACC} = 1.78), as calculated with the geochemical computer code PHREEQC[9]. Please note that within the bulk composition of the mixed microemulsions, the water cores constituted only 1.77% of the total microemulsion volume fraction, and thus the actual corresponding total maximum possible yield of $CaCO_3$ was ~1.3 mmol/L. However, this value is irrelevant in terms of the calculation of supersaturation indices above since, they have to be calculated assuming only the aqueous phase volume and not the total complex system, since $CaCO_3$ is insoluble in isooctane.

Prior to choosing the w=10 and salt concentration of 0.15 mol/L as the most adequate system, we tested several other compositions with respect to w at a constant surfactant concentration (before mixing): $5 \leq w \leq 15$, and $0.05 \leq$ [salt] ≤ 0.20 mol/L. Apart from w = 15 and $[CaCl_2]$ = 0.20 mol/L in all cases stable, single-phase optically-clear microemulsions formed. Upon mixing in all experiments again stable microemulsions formed and no variability in the reaction products was observed. We decided to use the w=10 and 0.15 mol/L ion concentration system as this yielded the highest possible amount of $CaCO_3$, while remaining safely within the microemulsion stability region (solubilization capacity). Furthermore, we also tested several other compositions outside the stability region (see also Note S1) to optimize the system as best as possible. These tests also included analyses using *in situ* and time-resolved turbidity measurements by UV-Vis spectroscopy (Uvikon XL) to determine the spectral features, which could be associated with the processes upon mixing of the two initial microemulsions (Fig. S6A). These tests revealed that the progress of reaction could be monitored through the evolution of the local maximum at ~275 nm (measured after 6 h). We have hence measured changes in absorbance as a function of time for three microemulsions of w=10 and different salt concentrations (Fig. S6B) and used these as a proxy for reaction progress. All the UV-Vis measurements were performed in a quartz cuvette with UV-VIS data collected every second.

Supporting Notes

Note S1. Structure of initial reverse micelles as derived from SAXS measurements.

All the morphological descriptions in this ESI note consider explicitly the composition a water-in-oil microemulsion in a tertiary system of aqueous phase/NaAOT/isooctane as described in Methods. A complete phase diagram of the system can be found elsewhere[10]. In water-in-oil microemulsions the minority aqueous phase (polar phase) is stabilised in isooctane (apolar "oil") by an ionic surfactant (NaAOT) in the form of nm-sized droplets (*i.e.* the reverse micelles, Fig. S1A). This stabilization is due to the structure of the surfactant, where a NaAOT molecule has a polar, hydrophilic primarily Na-sulfonate "head" group, which interacts with the polar aqueous phase, and two apolar, hydrophobic organic "tails", which interact with the apolar isooctane.

We fitted the SAXS patterns of the individual initial non-mixed microemulsions with a core-shell ellipsoid model[11] (Fig. S1B and Table S1). In this model the low polydispersity water core (with the axes a and b) is surrounded by a shell of monodisperse thickness composed of a monolayer of polar "head" groups of the AOT surfactant (thickness T_s)[11–13]. The remaining NaAOT "tails" are ignored in the structural model since their electron density closely matches that of the surrounding isooctane medium and hence does not contribute to the scattering contrast (Table S1). Form-free size distributions of water cores were found through a Monte Carlo fit implemented in MCSAS[1] using the ellipsoid core-shell form factor and the structural parameters from Table S1. The size and the geometry of the water cores in a microemulsion nanoreactor depend on the water-to-surfactant ratio w, and can be therefore changed/tuned accordingly[13,14] within the solubilisation capacity of the microemulsion (*i.e.,* maximum w at which phase separation in the microemulsion and an excess aqueous phase is observed, w_{max})[15–20] . Important to note is the fact, that although the concentration and speciation of salts dissolved in the aqueous phase have a limited impact on the size of the water pools, their presence considerably decreases w_{max}. In Fig. S1B, we show the scattering curves from two microemulsions with w=10, but containing different salt concentrations dissolved in the water cores. The two different scattering curves are identical at $q > 0.2$ nm^{-1}, but show a difference in

intensity (~15%) at low-q. This small difference is most likely caused by the presence of a minor population of tiny clusters of dimers or trimers in the Na_2CO_3-carrying micelles. As we further corroborate through the good fits with the structural model (Figs. S1B-D), in the two used microemulsions, the water droplets have the same size and shape. On the other hand, as we mentioned the solubilisation capacity of the two microemulsions is dependent on the concentration and nature of the counter-ion salts: our tests showed that at w = 10, the most adequate experimental conditions at which the microemulsion was stable, were at a maxmimum concentration of $CaCl_2$ of 0.2 mol/L. In contrast, for the Na_2CO_3 microemulsions, concentrations even higher than 1.0 mol/L could be used, without any visible phase separation. Conversely, for a constant concentration of salts (as used in the experiments *i.e.,* 0.15 mol/L), for $CaCl_2$ we could achieve a $w_{max} \sim 18$, whereas for Na_2CO_3 $w_{max} > 20$.

The reverse micelles exhibited relatively low polydispersity, but were not fully monodisperse. As previously demonstrated[11] for reverse micelles one has to consider simultaneously two types of polydispersity that could affect the size of the water cores: (1) polydispersity in the number of the NaAOT molecules building up a micelle, (2) shape polydispersity, when the ellipsoidal micelles cyclically "pulse" between the oblate and prolate forms, while preserving a constant volume of the water cores. Although, the analytical equations describing the scattering from such a system and including both kinds of polydispersity are available[11], the actual fitting with those equations does not yield satisfactory results. This is because an *a priori* assumption about the type of distribution(s) would have to be made, and one has to deal with mutual dependencies between fitting parameters. Therefore, we employed an alternative approach in which we used a Monte Carlo fitting procedures (Fig. S1B) implemented in the MCSAS software[1]. Our goal was to obtain the model-independent size distribution of the dimensions of the formed reverse micelles (Figs. S1C&D). This way we specified and constrain only the geometrical model of the micelle (core-shell ellipsoid) but derived the required structural information (details Table S1). In Figs. S1C&D we present the resulting histograms representing the size distributions of the dimensions of the ellipsoidal micellar water cores for the $CaCl_2$- and Na_2CO_3 -carrying microemulsions used in our experiments.

Note S2. Apparent growth rates of $CaCO_3$ globules

By analyzing and comparing the apparent growth rates derived from our *in situ* and time resolved LC-STEM and SAXS data we evaluated the influence of the confinement and electron beam exposure on the evolution of the globules shown in Fig. 1 (SAXS) and Fig. 2 (LC-STEM) in the main text. Although such a temporal and spatial juxtaposition is often difficult because of the differences in the probing volumes accessible to each the two techniques (1-100 nm^3 for STEM and 10 μm^3 - 1 mm^3 for SAXS), our data sets allowed us to carry out a comparison. Firstly, the scattering features in our SAXS data that correspond to the individual micelles and those that correspond to the growing globules are reflected in two highly separate regimes in q (low-q < 0.2 nm^{-1} and high-q > 0.2 nm^{-1}; Fig. 1 main text). The contrast is clear because even a small number of larger objects will strongly affect the scattering at low-q, because the intensity scales with the square of the volume of such scatterers. Thus, the shape of the scattering patterns at q < 0.2 nm^{-1} after ~ 20 min (which corresponds with the observable onset of globule growth; see arrow Fig 1 main text) indicates that the size of the growing objects fell outside the q-range throughout the entire growth process *i.e.,* once the intensity started increasing at low-q typically no Guinier region was observed. This indicates that the individual large scatterers (the globules) were growing in size very rapidly to a diameter >150 nm and beyond. Hence, the continuous increase in scattering intensity throughout the whole observation period (up to 180 min) originated primarily from the growing number density of large scatterers and not their gradual growth in size. This matches with our LC-TEM observations (Fig. 2 in the main text) that revealed that the growth of the globules, once visible in the images, proceeded extremely fast (within 180 s once visible). Nevertheless, the comparison between LC-STEM and SAXS data also showed that the overall evolution in the LC-STEM experiments occurred orders of magnitude faster than in the SAXS experiments (< 5 min *vs.* ~1.5 h). Hence, although the growth rate of the individual large objects/globules was very rapid in both experiments (a few minutes *per* globule), inevitably the difference in temporal evolution must be attributed to the "rate of appearance" of the individual new globules in SAXS *vs.* LC-STEM. We cannot exclude the possibility that in the LC-STEM images, the high "rate of appearance" of new globules could be related to electron beam-sample interactions or confinement. In all our LC-STEM work we kept the electron dose as

low as possible and at least visually no obvious interactions between the growing globules and the electron beam or changes in the globule behaviors were observed. On the other hand, the confined sample environment used for the *in situ* liquid cell microscopic imaging was characterized by a high surface-to-volume ratio in contrast to the bulk *in situ* scattering measurements. Both confinement and beam-interactions at the small scale could promote a more effective formation of hydrophobic globules in the LC-STEM set up compared to the bulk scattering experiments. These could thus explain the observed difference between the two characterization methods.

Note S3. Ex situ imaging and analysis of the morphologies of dried $CaCO_3$ microemulsions.

Ex situ TEM images of the bulk $CaCO_3$ microemulsion that were reacted for 3 h and that were deposited onto a TEM grid and washed with pure isooctane to remove an excess surfactant (see also Methods) are shown in Fig. S5. The image reveals sub-500 nm in diameter agglomerates composed of smaller primary particles of 10-15 nm in diameter. The selected area electron diffraction (SAED) from these particles indicated that the agglomerates were composed of nanocrystalline vaterite (inset I in Fig. S5A see also Fig. S4). High-resolution images (Fig. S5B), suggest that all individual primary particles within the agglomerates had similar crystallographic orientations, as also observed during the *in situ* crystallization (Fig. 3 in the main text). This can be deduced from the continuous lattice fringes extending across different individual primary particles (inside the box in Fig. 3B). Important to note is the fact that in contrast to the LC-STEM imaging, in these HR-TEM images we see crystallization that was most likely induced due to drying and / or due to the high vacuum conditions of the TEM column and/or to a certain extent due to the interaction with the beam during the actual imaging. The latter effect was evidenced by the increase in contrast of the lattice fringes, when we compared consequent images from the same area and their FFTs (inset I in Fig. S5B). The *d* spacing of the lattice fringes corresponded to vaterite (inset II in Fig. S5B, Fig. S4, Table S2).

Note S4. Number of ions per water core

In order to prepare a microemulsion of w=10 from 0.1 mol/L NaAOT in isooctane, we typically mixed 0.18 mL of the aqueous phase/10 mL of the surfactant solution in oil. The mean radius of the water core was ~1.7 nm (see Note 1), hence for the range of radii from 1.5 - 2 nm the volume of the individual water cores was ~14.1 – 33.5 nm^3. By knowing the total volume of the aqueous phase and the volume of an individual micelle, we could calculate the total number of micelles in our system (0.18 mL of water) to be ~ $0.54 \cdot 10^{19}$ - $1.27 \cdot 10^{19}$. In this system, the total number of moles of each salt in a 0.15 mol/L solution was accordingly equal to $2.7 \cdot 10^{-5}$ moles/microemulsion, while the total number of "undissociated salt species"/micelle was equal to the number of moles/microemulsion multiplied by Avogadro number and divided by the total number of micelles. Hence, for each individual ions we obtain: $[Ca^{2+}]$ = 1.23-3.03; $[Na^{+}]$ = 2.46-6.06; $[Cl^{-}]$ = 2.46-6.06; $[CO_3^{2-}]$ = 1.23-3.03 ions/micelle. The mixing of the individual microemulsions to start an experiment naturally halves these values. Although these are average values, one could actually expect a Poisson-like distribution of the number of ions across the water cores, since the micelles can exchange their contents with each other.

Supporting References

1 I. Bressler, B. R. Pauw and A. F. Thünemann, McSAS: software for the retrieval of model parameter distributions from scattering patterns., *J. Appl. Crystallogr.*, 2015, **48**, 962–969.

2 K. Momma and F. Izumi, VESTA 3 for three-dimensional visualization of crystal, volumetric and morphology data, *J. Appl. Crystallogr.*, 2011, **44**, 1272–1276.

3 D. L. Graf, Crystallographic tables for the rhombohedral carbonates, *Am. Mineral.*, 1961, **46**, 1283–1316.

4 S. R. Kamhi, On the structure of vaterite CaCO3, *Acta Crystallogr.*, 1963, **16**, 770–772.

5 J. Wang and U. Becker, Structure and carbonate orientation of vaterite (CaCO3), *Am. Mineral.*, 2009, **94**, 380–386.

6 H.-J. Meyer, Uber Vaterit und seine Struktur, *Angew. Chemie*, 1959, **71**, 678.

7 E. Mugnaioli, I. Andrusenko, T. Schüler, N. Loges, R. E. Dinnebier, M. Panthöfer, W. Tremel and U. Kolb, Ab-initio-Strukturbestimmung von Vaterit mit automatischer Beugungstomographie, *Angew. Chemie*, 2012, **124**, 7148–7152.

8 R. Demichelis, P. Raiteri, J. D. Gale and R. Dovesi, A new structural model for disorder in vaterite from first-principles calculations, *CrystEngComm*, 2012, **14**, 44–47.

9 D. L. Parkhurst and C. A. J. Appelo, *Description of input and examples for PHREEQC version 3: a computer program for speciation, batch-reaction, one-dimensional transport, and inverse geochemical calculations*, US Geological Survey, 2013.

10 B. Tamamushi and N. Watanabe, The formation of molecular aggregation structures in ternary system: Aerosol OT/water/iso-octane, *Colloid Polym. Sci.*, 1980, **258**, 174–178.

11 R. Hilfiker, H. F. Eicke, W. Sager, C. Steeb, U. Hofmeier and R. Gehrke, Form and structure factors of water/AOT/oil microemulsions from synchrotron SAXS, *Berichte der BunsenGesellschaft*, 1990,

94, 677–683.

12 E. Y. Sheu, S. H. Chen and J. S. Huang, Structure and growth of bis(2-ethylhexyl) sulfosuccinate micelles in aqueous solutions, *J. Phys. Chem.*, 1987, **91**, 3306–3310.

13 D. I. Svergun, P. V. Konarev, V. V. Volkov, M. H. J. Koch, W. F. C. Sager, J. Smeets and E. M. Blokhuis, A small angle x-ray scattering study of the droplet--cylinder transition in oil-rich sodium bis(2-ethylhexyl) sulfosuccinate microemulsions, *J. Chem. Phys.*, 2000, **113**, 1651–1665.

14 M. P. Pileni, Reverse micelles as microreactors, *J. Phys. Chem.*, 1993, **97**, 6961–6973.

15 G. A. Van Aken, J. T. G. Overbeek, P. L. De Bruijn and H. N. W. Lekkerkerker, Partitioning of Salt in Winsor II Microemulsion Systems with an Anionic Surfactant and the Consequences for the Phase Behavior, *J. Colloid Interface Sci.*, 1993, **157**, 235–243.

16 B. Bedwell and E. Gulari, Electrolyte-moderated interactions in water/oil microemulsions, *J. Colloid Interface Sci.*, 1984, **102**, 88–100.

17 R. Leung and D. O. Shah, Solubilization and phase equilibria of water-in-oil microemulsions: II. Effects of alcohols, oils, and salinity on single-chain surfactant systems, *J. Colloid Interface Sci.*, 1987, **120**, 330–344.

18 A. Derouiche and C. Tondre, Correlation between maximum water/electrolyte solubilization and conductivity percolation in AOT reverse micelles, *J. Dispers. Sci. Technol.*, 1991, **12**, 517–530.

19 K. Hamada, T. Ikeda, T. Kawai and K. Kon-No, Ionic Strength Effects of Electrolytes on Solubilized States of Water in AOT Reversed Micelles, *J. Colloid Interface Sci.*, 2001, **233**, 166–170.

20 J. J. Silber, A. Biasutti, E. Abuin and E. Lissi, Interactions of small molecules with reverse micelles, *Adv. Colloid Interface Sci.*, 1999, **82**, 189–252.